Laser-generated focused ultrasound transducer using a perforated photoacoustic lens for tissue characterization

JEONGMIN HEO,[1,4] DEBLINA BISWAS,[1,4] KYU KWAN PARK,[1] DONGHEE SON,[1] HUI JOON PARK,[2,3,5] AND HYOUNG WON BAAC[1,6] (iD)

[1]*Department of Electrical and Computer Engineering, Sungkyunkwan University, Suwon 16419, Republic of Korea*
[2]*Department of Organic and Nano Engineering, Hanyang University, Seoul 04763, Republic of Korea*
[3]*Human-Tech Convergence Program, Hanyang University, Seoul 04763, Republic of Korea*
[4]*These authors equally contributed to this work*
[5]*huijoon@hanyang.ac.kr*
[6]*hwbaac@skku.edu*

Abstract: We demonstrate a laser-generated focused ultrasound (LGFU) transducer using a perforated-photoacoustic (PA) lens and a piezoelectric probe hydrophone suitable for high-frequency ultrasound tissue characterization. The perforated-PA lens employed a centrally located hydrophone to achieve a maximum directional response at 0° from the axial direction of the lens. Under pulsed laser irradiation, the lens produced LGFU pulses with a frequency bandwidth of 6–30 MHz and high-peak pressure amplitudes of up to 46.5 MPa at a 70-μm lateral focal width. Since the hydrophone capable of covering the transmitter frequency range (~20 MHz) was integrated with the lens, this hybrid transducer differentiated tissue elasticity by generating and detecting high-frequency ultrasound signals. Backscattered (BS) waves from excised tissues (bone, skin, muscle, and fat) were measured and also confirmed by laser-flash shadowgraphy. We characterized the LGFU-BS signals in terms of mean frequency and spectral energy in the frequency domain, enabling to clearly differentiate tissue types. Tissue characterization was also performed with respect to the LGFU penetration depth (from the surface, 1-, and 2-mm depth). Despite acoustic attenuation over the penetration depth, LGFU-BS characterization shows consistent results that can differentiate the elastic properties of tissues. We expect that the proposed transducer can be utilized for other tissue types and also for non-destructive evaluation based on the elasticity of unknown materials.

1. Introduction

Ultrasound (US) is predominantly used in clinical medicine for diagnosis and therapy [1]. Various biomedical applications, such as ultrasonic therapy [2,3], tissue characterization [4–6], and ultrasonic imaging [7], have leveraged its unique ability to penetrate tissues noninvasively and deeply. Tissue characterization frequently utilizes acoustic frequency ranges, which interact with scatterers present in the tissue and create echoes of the incident US waves. The most common approach representing the backscattered (BS) information is the B-mode imaging that is reconstructed using the US signals (*i.e.*, A-mode signals) reflected from the tissue [1,6], which provides qualitative information about the tissue through contrast-based ultrasound images. However, other significant features of the US-BS signal (*e.g.*, frequency and phase) could provide useful quantitative information about the mechanical, acoustical, and structural properties of the tissue through the application of frequency-spectral analysis [8–10]. These properties include acoustic attenuation, sound speed, BS coefficient, scatterer diameter, and concentration, which

serve as markers for different diseases. In this context, US-BS signal analysis has recently attracted substantial attention [8].

This technique requires US irradiation into tissue samples and subsequent acquisition of the BS signal. The center frequency and bandwidth of the US transmitter determine the tissue penetration depth and quantitative information (*i.e.*, tissue structural and mechanical properties) [11]. Conventionally, piezoelectric transducers have been used for US-BS signal analyses over a variety of applications (*e.g.*, blood coagulation studies, non-destructive estimation of cell concentration, detecting apoptosis, monitoring cell viability, and estimation of collagen fiber density), including tissue characterization as well [6,12]. These analyses have been performed using transducers with low-MHz center frequencies (1~7 MHz) and bandwidths (64~80%), adopting a planar configuration for the tissue characterization [13–15]. These conventional US transducers provided quantitative information about bulk changes in structural and mechanical tissue properties. However, their ability to identify minute changes in tissue properties was limited [16] possibly due to the use of narrow-bandwidth US sources covering restricted frequency spectra near a few MHz [17,18]. Such minute changes in tissue properties, especially mechanical properties, can signal early-stage disease; thus, the quantitative assessment to changes in these mechanical properties could potentially reduce mortality by facilitating early-stage diagnosis [19]. For example, in the case of fatty liver disease, liver elasticity can vary significantly due to increased fat content, which has been extensively studied using both US-BS signal detection and US elastography [20–23]. However, conventional US-BS based studies have been restricted to the developed stages of fatty liver disease [24]. Despite promising outcomes, US elastography requires an additional displacement source for generating tissue displacement, which may restrict specific in-vivo conditions [25]. Therefore, a non-contact US transducer with broadband and high-frequency performance would substantially improve the ability to characterize tissue elasticity.

Focused photoacoustic (PA) transmitters, also referred to as PA lenses, are a promising alternative to conventional piezoelectric transmitters and have recently been developed using a carbon nanotube (CNT)-polydimethylsiloxane (PDMS) composite film coated on a concave lens substrate. Under the excitation of a few-nanosecond pulsed laser beam, the PA lens produces laser-generated focused ultrasound (LGFU) that exhibits a high-pressure amplitude of tens of MPa and a broad frequency bandwidth of 5–30 MHz (6 dB roll-off) at a tight focal zone (< 100 μm) [26]. Owing to these unique features, PA lenses have been used for various therapeutics at microscale precision, such as lithotripsy, drug delivery, and soft-tissue fragmentation [26,27]. The high-frequency and spatially confined characteristics of LGFU are attractive not only for therapeutic applications that have been realized so far, but also possibly for tissue characterization, for which it could overcome the limitations of conventional transducers. The high-pressure output of LGFU can deeply penetrate tissues overcoming intrinsic attenuation of US waves.

We propose a broadband ultrasonic transducer for differentiating biological tissues, which consisted of a perforated-PA lens with a 25-mm diameter, a 15.57-mm radius of curvature, and a 2-mm central hole diameter coupled with a polyvinylidene fluoride (PVDF) piezoelectric probe hydrophone. The perforated PA lens enables the placement of the needle-shaped probe hydrophone in the central hole of the lens such that the US-BS signals from the sample are detected by the hydrophone aligned in parallel with the axial direction of the spherical lens. For focused ultrasound generated from the PA lens, this unique structure provides highly sensitive US-BS signal detection through a maximized directional response at 0° from the axial direction of the lens [28]. Then, the targeted tissues demonstrate distinct differences in elasticity, which would be useful to tissue characterization. In this study, the hybrid transducer fabricated using the perforated PA lens is characterized in terms of the signal frequency, the focal dimension of LGFU, and the pressure amplitude. The time-domain US-BS signals from a glass (reference) specimen and excised tissue samples (fat, skin, muscle, and bone) are measured. Their corresponding

frequency spectra are obtained by applying the Fast Fourier Transformation (FFT). The frequency-spectral parameters of the tissues, such as the mean frequency and spectral energy, are then used to depict change in their elastic property.

2. Materials and methods

2.1. Fabrication of CNT-PDMS composite films

We prepared a CNT solution in which CNT powders (10–30 nm in diameter, HWNANO Inc., China) were dissolved in toluene. This solution was spin-coated onto a concave surface of perforated lens (1000 r.p.m. for 30 sec) and then dried out in room temperature for leaving CNTs only on the substrate. PDMS (Sylgard 184, Dow corning Inc., USA) was prepared by mixing a silicon elastomer base with a curing agent (10:1 ratio), and then diluted the mixture by using hexane (a weight ratio of 1:2). The diluted PDMS was spin-casted on the CNT-coated lens substrate (2000 r.p.m. for 1 min), followed by a curing process on a hot plate (100 °C for an hour).

2.2. LGFU transducer with a perforated PA lens and a piezoelectric probe hydrophone

The LGFU transducer consisted of a piezoelectric probe hydrophone (PVDF; 1-mm sensing diameter and 1.5-mm outer diameter; Precision Acoustics Inc., UK) and a perforated PA lens with a 25-mm diameter and a 15.57-mm radius of curvature (approximate focal length), as shown in Fig. 1. The hydrophone exhibited a broad-frequency bandwidth of 0.2–20 MHz and a mean sensitivity of 850 mV/MPa over the range of 2–12 MHz [28]. These parameters enabled the measurement of a US-BS signal with a dynamic pressure amplitude and frequency of approximately 20 MPa and 20 MHz, respectively. The perforated PA lens was fabricated for LGFU by coating a concave lens substrate with a CNT-PDMS composite film, as shown in the inset of Fig. 1 (perforated BK7 lens substrates purchased from Sunghunoptics Inc., KR). The CNT exhibited excellent light absorption of >90% that can be controlled by a CNT density in the PDMS matrix.
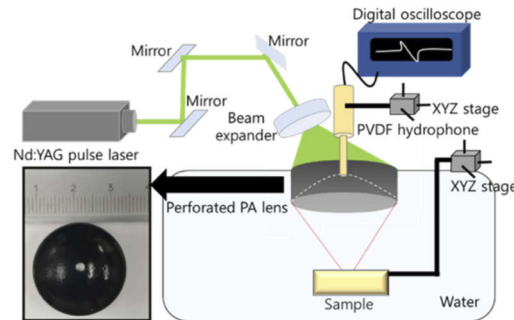
Fig. 1. Experimental setup of the US transducer based on a perforated PA lens and PVDF hydrophone. The inset shows the top view of the perforated PA lens (diameter: 25 mm, radius of curvature: 15.57 mm, central hole diameter: 2 mm). The right schematic shows that LGFU was produced by pulsed laser excitation onto the perforated PA lens, then propagating onto the tissue sample. The PVDF hydrophone detected the US-BS signal from the sample. The signal was stored in the digital oscilloscope.

The absorbed light energy was then converted to thermal energy that rapidly diffused into the surrounding PDMS with a high thermal expansion coefficient [27]. The instantaneously heated PDMS produced US waves owing to the PA effect. The US was focused, as per the geometric focal properties of the lens, on the area of the concave lens surface coated with the CNT-PDMS

film. The diameter of perforation in the glass lens could be customized in fabrication within the range of 0.5 to 2 mm. Here, we used a 2-mm diameter perforation through the whole concave substrate, which enabled the placement of the PVDF hydrophone tip [28]. This configuration provided sensitive US-BS signal detection due to the high sensitivity of the PVDF hydrophone aligned at 0° with the axial direction of spherical lens. The hydrophone had a directional response with 6-dB reduction at 9° tilted from the central axis in the 15-MHz frequency range for a relative amplitude of 0 dB at 0° [28].

The LGFU was produced under pulsed laser excitation of the perforated PA lens (Nd:YAG, 532-nm wavelength, 6-ns pulse width; Litron Laser, UK). Due to the length of straight needle-shaped hydrophone (20 mm), there is a long protrusion out of the planar side of lens that inevitably blocks some part of the pulsed laser beam from irradiating onto the lens. In order to reduce the irradiation loss especially near the center of Gaussian laser beam, the laser beam was incident with a tilt angle of 35° from the lens axis, leaving a narrow shadow line behind on the lens surface. We employed a fiber-optic hydrophone (for focal signal detection) [29] and a laser shadowgraph [30] to quantitively characterize the LGFU by observing the frequency, pressure amplitude, wavefront, and focal spot size. The PVDF hydrophone in the center of the perforated PA lens then acquired US-BS signals from a glass (a rigid reflector used as a reference) and fresh porcine tissues (skin, muscle, and fat from belly, and rib bone) purchased from butcher shop. The PVDF hydrophone was located 15 mm from the LGFU focal point and connected to a digital storage oscilloscope (500-MHz bandwidth; WaveSurfer 452; Teledyne LeCroy Inc.) that could acquire the BS signal at a sampling rate of 2 GS/s and store the data for later use.

2.3.   *Laser-flash shadowgraphy for visualization of LGFU and US-BS waves*

In order to observe LGFU propagation and align the focal zone of LGFU with a target tissue region, we used a laser-flash shadowgraphy technique [30]. A delay generator (DG535, Stanford Research System Inc., USA) was employed to trigger two laser pulses, one from a main pulsed laser beam for PA lens excitation and the other from an additional pulsed laser beam used as a probe to generate shadowgraphs (532-nm wavelength and 5-ns pulse width; Continuum Minilite-I, USA). The probe beam was aligned in a perpendicular direction to the PA lens axis, which enables to take instantaneous images that are recorded in the CCD camera (Point grey camera, USA). In this arrangement, the probe beam passing through the focal zone of LGFU is modulated in response to pressure-induced variation of the refractive index of water, resulting in bright/shadow regions on the CCD camera [31].

2.4.   *Spectral sensing method for differentiating biological tissues*

US-BS signal spectral analysis is a promising technique for differentiating tissues based on their mechanical properties [32,33]. To verify the spectral sensing capability of our transducer, the time-domain US-BS signals of the tissue samples were measured and averaged 200 times before storage in the digital oscilloscope. Then, we performed the FFT to obtain the frequency spectrum of the US-BS signal. The spectral parameters of mean frequency and spectral energy were obtained for the quantitative tissue characterization. The mean frequency (f_m) [34] and the spectral energy (E_s) [35,36] were calculated from the following formula:

$$f_m = \frac{\sum_{j=1}^{M} f_j P_j}{\sum_{j=1}^{M} P_j} \tag{1}$$

$$E_s = \sum_{n=-\infty}^{\infty} [X(n)]^2 \tag{2}$$

where f_j, P_j, M, and $X(n)$ are the frequency of the US-BS signal, the power-spectral magnitude of US-BS signal, the length of frequency bin, and the FFT spectrum output of US-BS signal,

respectively. In this study, E_s was calculated with a frequency range of 0–20 MHz corresponding to the bandwidth of PVDF hydrophone. In order to evaluate the spectral energy strength over a specific frequency regime of interest, a relative spectral energy can be calculated as following: *i.e.*, low frequency (0–5 MHz) and high frequency (5–10 MHz) by the following equation:

$$E_{LS} = \frac{E_L}{E_S} \tag{3}$$

$$E_{HS} = \frac{E_H}{E_S} \tag{4}$$

where E_L, E_H, E_{LS}, and E_{HS} are the spectral energy over a low frequency regime of 0–5 MHz, a high frequency regime of 5–10 MHz, the relative proportion of E_L within E_S, and a relative proportion of E_H within E_S. From the relative strength of spectral energy (E_{LS} and E_{HS}), we can find out which frequency component dominantly contributes to the US-BS signal. Thus, a quantitative change in the spectral energy can be evaluated at a specified frequency regime, which delineates critical information about different tissue characteristics, *e.g.*, including elasticity.

3. Results and discussion

### 3.1. Characterization of PA transmitter for LGFU

LGFU propagation from the perforated PA lens was characterized by visualizing wavefronts, together with detecting focal signals. Under pulsed laser irradiation, the LGFU was transmitted initially from the spherical surface of the concave lens substrate with a central hole to the focal point. The LGFU wavefronts were captured using the laser shadowgraphy as shown in Fig. 2. The dark curved shadow line in each figure in Fig. 2 corresponds to the wavefront, and the green background is the water medium. In detail, the bright line following the dark shadow of each wavefront is resulted from the rarefactional phase of LGFU lowering the density of water molecules. The wavefronts are shown at different propagation moments; 8.5, 9.5, and 10.5 μs for Figs. 2(a), 2(b), and 2(c), respectively (here, 0 μs means the moment of LGFU transmission at the lens surface). Figure 2(c) shows the LGFU arrival approximately at the focus, which confirms the focal length of ~15.57 mm. Notably, Fig. 2(a) shows that the center of the wavefront is slightly narrower than the area near the curved wavefront due to the absence of US generation at the center hole in the lens. Then, the wavefront center becomes gradually thicker as closer to the focus as shown in Figs. 2(b) and 2(c). The tightly focused US is observed in Fig. 2(c), leading to the lateral focal dimension of ~80 μm.
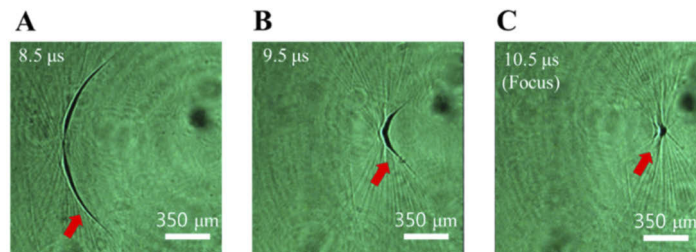
Fig. 2. Visualization of propagating wavefronts by the laser-flash shadowgraphy. Each wave motion was captured at a different propagation moment. The LGFU wave, transmitted at 0 μs, reached the lens focal point at 10.5 μs. The red arrow indicates the LGFU wavefront in each moment.

Then, the PVDF hydrophone was located at the center of the perforated PA lens, making a hybrid US transducer configuration for tissue characterization later. Due to the long hydrophone

that blocks some part of laser irradiation onto the planar side of lens, the narrow shadow line on the lens surface (Fig. 3(a)) could thus induce a lower pressure amplitude because the CNT-PDMS composite film did not undergo laser excitation. For the non-excited zones at the central hole and the line-shaped shadow on the planar side of lens, each loss area corresponds to 0.6 and 3.7%, respectively, for the full spherical area available from the lens substrate without any perforation and shadow.
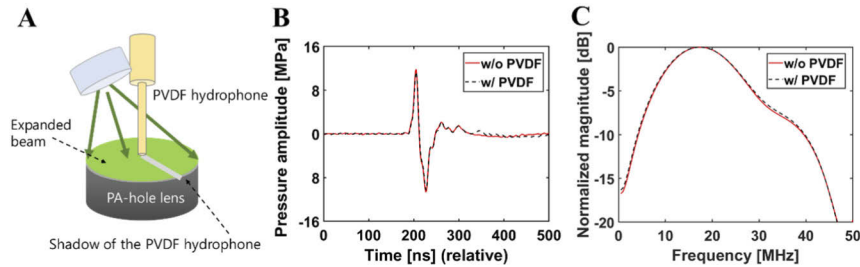

Fig. 3. LGFU characterization of the perforated PA lens. (a) Schematic of the laser beam pattern irradiated on the perforated PA lens that has the shadow line caused by the hydrophone placement; (b) Time-domain LGFU waveforms at the focus; (c) Frequency spectra obtained from the time-domain waveforms in (b).

In order to evaluate possible performance degradation due to the placement of hydrophone, we obtained each signal in the focal field using the fiber-optic hydrophone, generated from the perforated PA lens with and without the PVDF hydrophone. For LGFU characterization, the pulsed laser energy of 2 mJ was used. In the center of the focal zone (the highest-pressure amplitude), both focal signals exhibited a similar waveform with a temporal width of 21 ns (peak to peak) (Fig. 3(b)). The pressure amplitude differs slightly between two cases with and without the PVDF. At the positive (+) peak, the pressure amplitudes of 11.94 and 12.5 MPa were obtained, respectively, and at the negative (−) peak, 10.8 and 11.25 MPa, respectively (Fig. 3(b)). According to the pressure amplitude gap, the pressure loss caused by the hydrophone shadow was only 4~4.5%, agreeing with the loss area of 4.3% that is resulted from the addition of 0.6 and 3.7% as explained above. Then, FFT signal processing was performed to these time-domain signals, which led to a frequency bandwidth of 6–30 MHz (center frequency: 17 MHz) obtained for both cases with negligible spectral difference (Fig. 3(c)).

The focal spot dimension of the PA lens with the PVDF was measured as 70 μm in the lateral direction and 270 μm in the axial direction, as shown in Figs. 4(a) and 4(b). The full width at half maximum (FWHM) size measured here by translating the fiber-optic hydrophone at the focal zone almost agrees with the focal zone dimension (~80 μm) observed by the laser-flash shadowgraphy as confirmed in Fig. 2(c).

The frequency and focal dimension characteristics of perforated PA lens are compared to those without a central hole reported elsewhere (Table 1). All of the previous PA lenses in Table 1 were based on a carbon nanoparticle-PDMS composite film capable of producing LGFU by pulsed laser irradiation with a 6–10 ns pulse width. LGFU frequency characteristics are determined by the laser pulse width and the film thickness [27]; LGFU has typically produced a center frequency of >10 MHz and a focal spot size of approximately 100 μm in the lateral direction and a few-fold longer in the axial direction. The table suggests that the current perforated PA lens owns a significantly high center frequency (17 MHz) and a tight focal width (laterally 70 μm and axially 270 μm) at a longer focal length of ~15.57 mm, although the spherical PA transmitter includes the non-excited zones at the central hole and the line-shaped shadow due to the detector alignment.
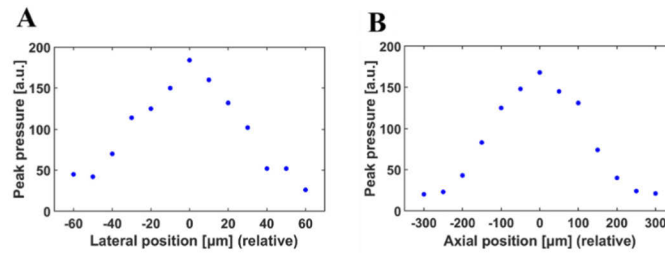
Fig. 4. Characterization of spatial focal profiles of LGFU (with fiber-optic hydrophone) along the (a) lateral and (b) axial directions. Each dot means the peak positive pressure amplitude at each position.

Table 1. Comparison of PA lenses.[a]

PA transmitter	D (mm)	r (mm)	f_N	Laser pulse width (ns)	f_c (MHz)	Lateral focus size (μm)
CNT-Au-PDMS [26]	6	5.5	0.91	6	15	75
CSNP-PDMS [37]	6	4.7	0.78	6	14	100
CSNP-PDMS [38]	5	3	0.6	10	10	150
CSNP-PDMS [39]	2	1.3	0.65	10	12	N/A
CNT-PDMS [40]	15	9.2	0.61	6	15	100
Current PA lens	25	15.57	0.62	6	17	70

[a]D: diameter; r: radius of curvature; f_c: center frequency; f_N: f-number; CSNP: candle soot nanoparticle.

For non-destructive tissue characterization, LGFU amplitudes at the focus should not exceed the threshold to induce acoustic cavitation in the tissue. However, the pressure amplitudes should be high enough to overcome intrinsic attenuation that severely increases with acoustic frequency [41]: $\alpha = \alpha_0 \cdot f^b$ (dB·cm^{-1}·MHz^{-1}) where α, α_0, f, and b are the amplitude attenuation coefficient, the attenuation factor, the acoustic frequency, and the power-law exponent for the attenuation coefficient, respectively. In order to avoid tissue damage induced by cavitational disruption and thus to ensure non-destructive analysis, the incident pulsed laser energy into the PA lens should be lower than a certain laser energy threshold (E_{th}) that makes LGFU-induced cavitation at focus [26].

In our PA lens with the perforation, a pulsed laser energy to induce cavitation at a rigid boundary, $E_{th(rigid)}$, was determined to be 2.4 mJ/pulse (fluence: 0.38 mJ/cm^2; *i.e.*, a pulsed laser energy per a curved surface area) on the end face of the fiber-optic hydrophone. We note that this is the condition for cavitation at an impedance-mismatched interface (water/glass) that can be generated by the negative peak of ~13 MPa. It is known that cavitation occurrence in a free-field condition or better impedance-matched conditions (*e.g.*, soft tissue/water) requires much stronger-pressure amplitudes in the negative phase of US waveform: *e.g.*, –15 MPa in the fat tissue and –26 MPa in the free-field of water medium, respectively [42,43]. The free-field cavitation in water by LGFU (*i.e.*, –26 MPa) has required an input laser energy $E_{th(free)}$ that is approximately 8–10 fold higher than $E_{th(rigid)}$ at the water/glass interface [44]. This makes an estimation of $E_{th(free)} = 19~24$ mJ/pulse for our perforated PA lens. For non-destructive tissue characterization with a soft tissue/water interface, this allows us to determine a safe input laser energy level into the PA lens not to cause cavitational disruption as ~11 mJ/pulse, corresponding to ~$0.5E_{th(free)}$, *i.e.*, a half of the threshold for free-field cavitation.

We also confirmed a pressure loss of PA lens due to the line-shaped shadow formed by the detector placement, as the input laser energy increases (Fig. 5). The (+) and (−) peak pressure amplitudes of the perforated PA lenses were compared with and without the hydrophone at the

center. While the (+) and (−) LGFU pressure amplitudes increased with the pulsed laser energy, the pressure loss lower than 4.7% was maintained with the detector placement at the perforation. Other aspects for the input laser energy versus the output pressure amplitude were similar with previous results reported elsewhere. These correspond to the nonlinear saturation behavior at the high-pressure regime of tens of MPa [45] and no measurable values for negative peaks above the laser energy higher than $E_{th(rigid)}$ due to the waveform distortion at the negative phase by the formation of cavitation at the detector surface [26,37,38].
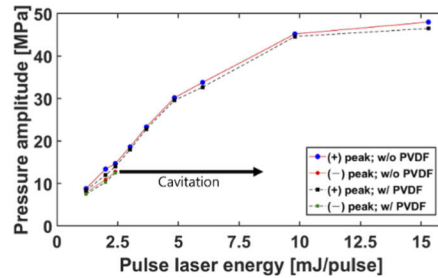

Fig. 5. Peak pressure amplitudes as a function of laser pulse energy with and without the PVDF hydrophone placement at the central hole. The amplitude gap between two curves is induced by the non-excited zone resulted from the hydrophone placement at the center of PA lens. The (−) pressure did not manifest above 2.4 mJ/pulse (fluence: 0.38 mJ/cm^2), which corresponds to approximately 13 MPa in the rarefactional phase, due to cavitation-induced signal distortion at the detector surface.

3.2. Biological tissue characterization

The US-BS signal was obtained and characterized for differentiating the tissues through the frequency-spectral analysis. As a reference for US-BS signal, we used a glass/water interface that provides a high acoustic reflectivity due to the acoustic impedance (Z) mismatch, resulting in a strong BS signal (Z_{glass} = 15 MRayl and Z_{water} = 1.5 MRayl) [46–48]. With the pulsed laser energy of 2 mJ, the PA lens produced LGFU with the positive peak of 11.9 MPa at focus. Figure 6(a) shows the incoming LGFU wavefront from the top to the bottom glass substrate whose interface is placed at the lateral focal plane. After arriving at the focus, the direction of wavefront propagation is flipped back to the upper side, making the spherical BS wavefront (Fig. 6(b)). Here, the dark shadow line appears clearly due to the strong compressive pressure, whereas the relatively weak BS signal manifests as the hazy wavefront. The US-BS signal was measured by using the PVDF hydrophone, shown as a single pulse with a temporal width of ∼50 ns (FWHM) in Fig. 6(b). Then, the time-domain signal was processed by FFT for characterization in the spectral domain (Fig. 6(c)), resulting in f_m = 6.55 MHz, E_{LS} = 0.46, and E_{HS} = 0.54, which were obtained by using Eqs. (1), (3), and (4). These spectral parameters from the glass/water interface were used as reference values for characterizing biological tissues.

We characterized excised porcine tissues *ex vivo* by using an input LGFU amplitude of 44 MPa (positive) at the tissue surface, which is produced by an input laser energy of 10 mJ/pulse to the PA lens, and then obtaining BS time-domain signals by the PVDF hydrophone. Figure 7(a) shows the shadowgraphs for the incoming and BS wavefronts in which the blue and red arrows indicate the direction of propagation. The BS wavefronts from all tissues (black shadows on bottom) appeared as relatively faint spherical contours for the incident ones. These propagated upwards (red arrows), resulting in signal waveforms measured by the hydrophone as shown in Fig. 7(b). This shows that the US-BS signal waveform was inverted for bone. This is due to large difference in acoustic impedances of water and bone [49]. Subsequently, in terms of pulsed widths of US-BS signals, the decrease in the tissue density leads to pulse width broadening.
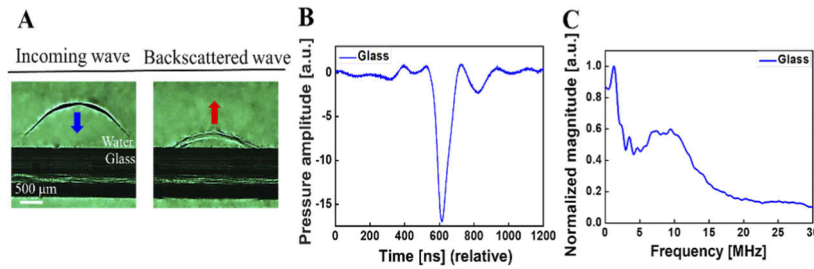
Fig. 6. (a) US wave propagation in the shadowgraphy images. The left image is the incoming wave, and the right image is the US-BS wave from the glass. The black curved shadow is the US wavefront in the water. (b) Time-domain US-BS signal from the glass; (c) Acoustic frequency spectrum converted from the time-domain signal in (b).

Figure 7(b) shows that the bone exhibits a significantly narrower width than the fat. This can be explained by interaction between incoming US and scatterers present in the tissue [50,51]. As a high-density tissue, the bone consists of scatterers densely packed in the specific volume of interest as compared to the fat that corresponds to a relatively low-density tissue [52].

Subsequently, these time-domain signals utilized to obtain corresponding frequency spectra (Fig. 7(c)) that were used to extract the spectral parameters of mean frequency and spectral energy. For fat, muscle, skin, and bone, we obtained $f_m = 0.95$, 2.8, 2.98, and 4.68 MHz, respectively. These differences in the mean frequencies imply that significant disparities exist in tissue elastic property, depending on the tissue types. The bulk modulus has been used as the quantitative parameter to indicate elastic property of biological tissues, as it represents the tissue resistance against uniform volumetric compression [53]. This property can be expressed as [54]:

$$B = \rho C^2 \tag{5}$$

where B, C, and ρ are the bulk modulus, the longitudinal sound speed, and the density of the tissue, respectively. Table 2 shows calculated bulk moduli for tissues and glass by using the above equation, together with the sound speed and the density reported elsewhere [55]. We can also obtain the relationship between the bulk modulus and the frequency characteristic of US-BS signal:

$$C = \frac{2\pi f}{k_w} \tag{6}$$

where k_w is the wavenumber and f is the acoustic frequency. For a constant wavenumber, the sound speed is linearly proportional to the frequency. Then, the combination of Eqs. (5) and (6) for a constant density implies that the mean frequency ($f = f_m$) increases with the bulk modulus. This is confirmed by comparing tissue properties as shown in Table 2. For example, the muscle has a higher bulk modulus (B_M) than the fat (B_F) by using Eq. (5). Such trend of $B_M > B_F$ is consistent with those of mean frequencies resulted from US-BS signals. The mean frequencies were 2.8 MHz in the muscle and 0.95 MHz in the fat. Similarly, other tissues also exhibited the similar trend of the mean frequency determined by bulk modulus, as summarized in Table 2. This demonstrates that our hybrid transducer enables to differentiate tissue types by using spectral parameters obtained from US-BS signals. However, the relation between the mean frequency and the bulk modulus in Table 2 does not exactly follow the square dependence that can be derived from Eqs. (5) and (6). In this study, we use the PVDF hydrophone with a finite frequency bandwidth of 0.2–20 MHz which does not entirely cover the LGFU bandwidth from the focal transmitter (6–30 MHz). This causes a possible loss in US-BS signal in terms of frequency-spectral amplitudes. Such limitation can be overcome by using a bandwidth-matched receiver or a receiver with a broader spectral coverage.
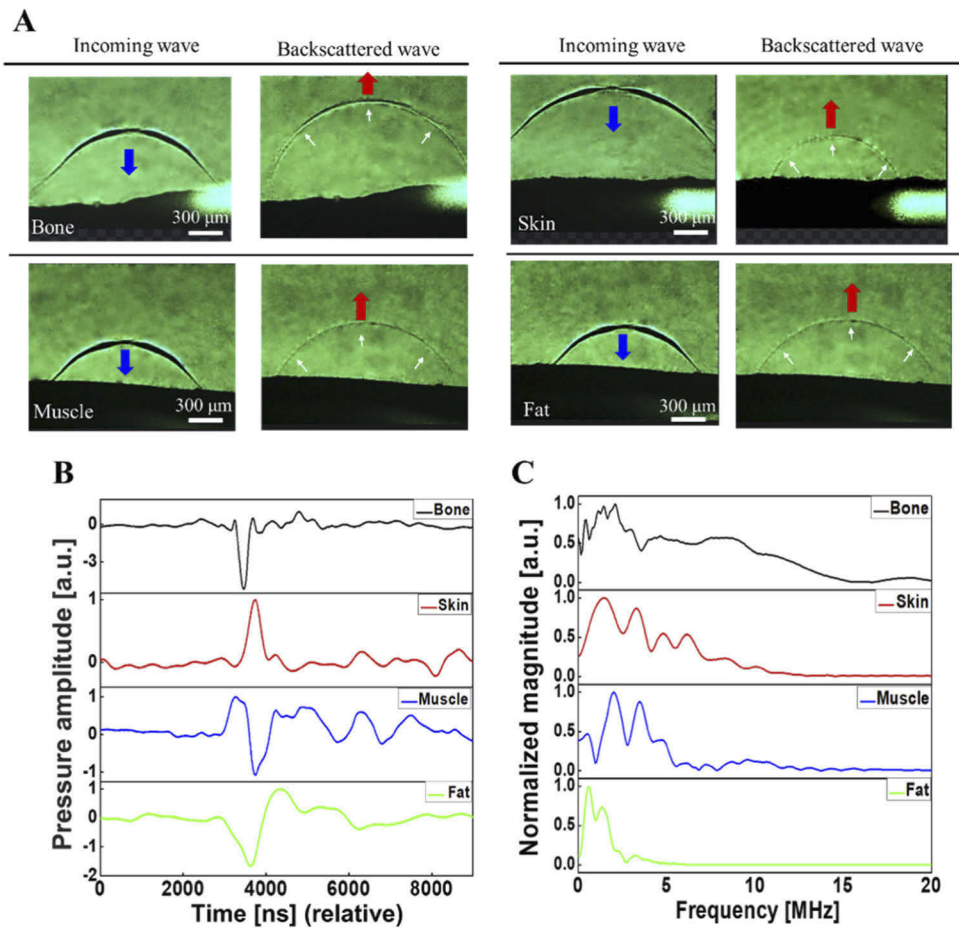
Fig. 7. (a) US wavefronts captured by using the laser-flash shadowgraphy. Incoming wave (LGFU) and US-BS wavefronts from excised porcine tissues. The white arrows indicate US-BS wavefronts (shown as faint contours). The red and blue arrows indicate the directions of wave propagation. (b) Time-domain US-BS signal from the tissues; (c) Normalized frequency spectra obtained from (b).

Table 2. Physical properties [55] and measured spectral parameters of the tissues and glass used as a reference.

| Tissue | Mean frequency (MHz) | Relative proportion of spectral energy[a] | | Density (kg/m³) | Sound speed (m/s) | Bulk modulus (GPa) (by Eq. (5)) |
		E_{LS}	E_{HS}			
Bone	4.68	0.60	0.35	1900	4000	30.4
Skin	2.98	0.83	0.16	1150	1730	3.44
Muscle	2.8	0.96	0.029	1065	1590	2.69
Fat	0.95	0.95	0.00018	950	1450	1.99
Glass (ref.)	6.55	0.46	0.54	2500	4540	51.52

[a]These are the proportion of spectral energy (normalized to the total spectral energy) over frequency ranges of $0 - 5$ and $5 - 10$ MHz for E_{LS} and E_{HS}, respectively, as defined in Eq. (3) and (4).

In addition to the mean frequency, we also characterized the relative spectral energy from a specific frequency bandwidth that can differentiate the tissue types based on elasticity. We defined two frequency bandwidths of 0–5 and 5–10 MHz, respectively, for E_{LS} and E_{HS}, respectively, to specify the relative proportion of spectral energy that is normalized to the total spectral energy over the US-BS frequency spectrum (0–20 MHz). This characterization is significant as E_{LS} and E_{HS} strongly depend on the concentration of scatterers which respond to the frequency range. As shown in Table 2, E_{LS} and E_{HS} of bone were obtained as 0.6 and 0.35, while fat is enriched more by the low-frequency components ($E_{LS} = 0.95$ and $E_{HS} = 0.00018$). Consistently with the above mean frequency result, this also indicates that the relative proportion of spectral energy over the high-frequency regime increases with the bulk modulus.

We performed depth-dependent tissue characterization by acquiring US-BS signals at tissue depths of 1 mm and 2 mm. This was performed by placing the focus of LGFU at 1- and 2-mm depth from the tissue surface. A sensing depth at a given focal plane was 270 μm, corresponding to the 6-dB spot dimension along the axial direction. The signals were compared with those obtained from the tissue surface (*i.e.*, 0 mm). This demonstrated that frequency spectra can identify tissue types in terms of mean frequency and relative spectral energy across the 2-mm depth. For example, f_m in the bone (4.67 MHz) was 4.7 times that of the fat (0.99 MHz) when the US-BS signals were acquired from the surface. For the 2-mm depth, the mean frequency was still 3.7-fold higher in the bone (3.46 MHz) than in the fat (0.94 MHz) as confirmed in Fig. 8(a). Such differentiation by the mean frequency, corresponding to the bulk modulus, was achieved, regardless of the assessment depth. On the other hand, f_m in the bone was shifted from 4.67 MHz at the surface to 3.46 MHz as the focus of LGFU with the 6-dB lateral and axial dimensions of 70 μm and 270 μm moves axially towards the tissue by 2 mm. We note that LGFU is strongly reflected from the bone surface (~88%), but still a significant amount of pressure amplitude is available for penetration into the bone and thus characterization. The reduced frequency is due to the acoustic attenuation dependent on the propagation depth and the acoustic frequency. The frequency-dependent attenuation coefficient α of the bone is higher than all the other tissue types used here (*e.g.*, bone: 20 dB·cm^{-1}·MHz^{-1}; fat: 0.6 dB·cm^{-1}·MHz^{-1} [55]). The decreasing behavior of f_m with the penetration depth agrees with the result reported elsewhere [52], confirming the variation of mean frequency depending on the depth and attenuation coefficient of tissues. However, such frequency shift of f_m to a lower value was not quite noticeable for the fat tissue between surface and 2-mm depth (0.95 and 0.93 MHz).
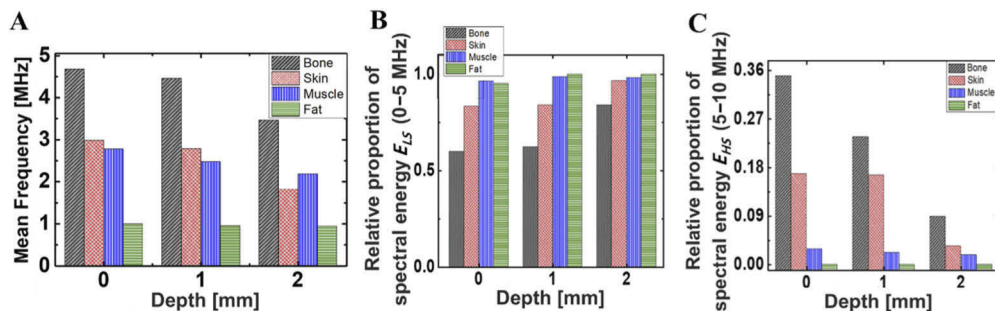
Fig. 8. Depth-dependent tissue characterization based on the US-BS frequency-spectral parameters: (a) f_m, (b) E_{LS}, and (c) E_{HS}. Note that (b) and (c) have different vertical scales. The relative proportion of spectral energy has the value between 0 and 1.

Particularly, f_m in the skin rapidly dropped from 2.98 MHz at the surface to 1.82 MHz at 2 mm which is even lower than that of the muscle at the same 2-mm depth. This is possibly due to the layered structure of skin consisting of the epidermis, dermis, and subcutaneous fat, each of which has different acoustic properties; *e.g.*, the sound speeds of epidermis and dermis are 1645 ± 42

and 1595 ± 41 m/s, respectively [56]. The layer with the slow sound speed would induce the low-frequency shift, following Eq. (6).

The relative spectral energy for all the tissue types also demonstrates significant differentiation as shown in Fig. 8(b) and (c). The ratio (E_{LS}) of the spectral energy over 0–5 MHz to the entire energy over the measurable bandwidth (0–20 MHz) showed a trend of bone < skin < muscle < fat, regardless of depth. A reverse trend of bone > skin > muscle > fat was observed in E_{HS} (5–10 MHz). For example, the US-BS signal from the bone surface consists of the spectral energy of 60% over 0–5 MHz and 35% over 5–10 MHz. However, this composition in the US-BS signal changed to 84% and 9%, respectively, at the 2-mm depth. This is because the high-frequency components (5–10 MHz) undergo higher attenuation with the increased depth, resulting in the significant drop in the relative proportion for 5–10 MHz. This manifests the increase in the relative spectral energy over the low-frequency range. Our characterization demonstrates that the bone can be clearly differentiated from the other tissues even at the 2-mm depth, despite the attenuation. The spectral characterization can be further extended to the range of 10–15 MHz to compare bone with the other tissues. This would lead to prominent differentiation in terms of relative strength, because the spectral energy in the other tissues has a negligible proportion over 10–15 MHz as shown in Fig. 7(c).

With an increased depth, increasing (E_{LS}) and decreasing (E_{HS}) trends were consistent for all tissues. However, the variation of E_{LS} and E_{HS} in the bone was more prominent than the variations in the other tissues. This is because the US-BS signal from the bone consists of high-frequency components initially at the surface which attenuate severely with the increased depth. For the muscle tissue, the US-BS signal from the surface consists of the spectral energy of 96% over 0–5 MHz and 2.9% over 5–10 MHz. This changed into 98% and 1.8% at 2 mm. Even smaller variation was obtained for the case of fat; 95% over 0–5 MHz and 0.018% over 5–10 MHz at the surface, and then changed into 99% and 0.015% at the 2-mm depth. As compared to the muscle and fat tissues, skin has more noticeable variation of E_{HS} over the 2-mm depth as shown in Fig. 8(c).

The mechanism of US interaction with scatterers which determines BS signal can be explained as follows. Here, we assume two comparative cases containing high- and low-density scatterers in volume as depicted in Fig. 9(a). For both cases, LGFU-BS signal waveforms would be obtained by taking the temporal convolution of the incoming LGFU pulse and an axial interaction zone scaled into the time domain. For the case 1 with high density, the LGFU wave is strongly scattered at the focal zone, resulting in a tightly confined BS pulse; schematically shown as the summation of narrow individual pulses from the high-density scatterers over τ_1. Whereas in the case 2 with low density, the LGFU scattering occurs over a relatively broader zone at the focus. This is due to the weak scattering amplitude caused by the low-density distribution of scatterers, which is shown with the summation of weak pulses over τ_2. Therefore, the temporal BS pulse width in the case 1 is narrower than in the case 2, together with the stronger peak pressure in the case 1, as shown in Fig. 9(b). As the time-domain BS pulse width is converted into the frequency domain, the frequency spectrum in the case 1 consists of broader and higher-frequency components than that in the case 2 (Fig. 9(c)). Such dependence of frequency components on tissue density was well confirmed by characterizing the relative spectral energy; *i.e.*, $E_{HS(bone)} > E_{HS(skin)} > E_{HS(muscle)} > E_{HS(fat)}$.

The proposed technique could be potentially useful to differentiate tissue types by characterizing the LGFU-BS signal that includes elasticity variation. Our approach relies on characteristic frequency parameters for such elastic property variation quantitatively. This is in contrary to conventional elastography techniques that obtain elastic modulus through tissue displacement. Our results promptly emphasize the advantage of broad bandwidth of LGFU transducer over conventional transducers operated in the low-frequency range (*e.g.*, <5 MHz) with narrow bandwidths. Transmitted LGFU pulses from the perforated lens have the center frequency of
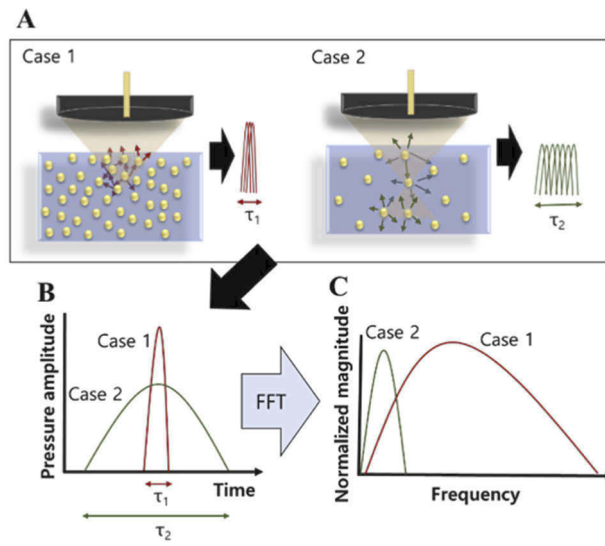
Fig. 9. Schematic diagrams to explain the mechanism of LGFU-BS. (a) For the incoming LGFU waves, two comparative cases are shown with high- and low-densities (defined as case 1 and 2, respectively). The BS amplitude and the pulse duration (τ) are determined by the temporal convolution of the incoming LGFU waveform and an axial interacting zone scaled into the time domain; (b) Time-domain BS pulses; (c) Acoustic frequency spectra corresponding to the time-domain BS pulses shown in (b).

17 MHz and the 6-dB bandwidth defined at 6 and 30 MHz. This allows to generate acoustic pulses with 21-ns width at the microscale focal spot. LGFU-BS signals are then received and characterized by the PVDF hydrophone located at the central hole of the lens. The PVDF hydrophone was placed in perpendicular to the sample in order to minimize angle-dependent variation in the US-BS signal characteristics, which is confirmed by the laser shadowgraphy. Currently, we have used the commercial needle-shaped hydrophone as a receiver, but the perforated region at the center of lens can be extensively utilized by mounting with other acoustic receivers or endoscopic devices (*i.e.*, optical monitoring) whose diameter are less than 2 mm. The diameter of central region can be further enlarged by a few mm in diameter, if needed for a device to be located, which is still available in the expense of a moderate loss of the output pressure.

In the perforated geometry of LGFU transducer, the PA lens is optically excited in an off-axis manner. This causes a non-uniform optical fluence arriving at the surface of PA lens. Basically, an output pressure from the PA lens is resulted from the summation of illuminated surface pressure. This means that the asymmetric illumination in our geometry can lower output LGFU amplitudes as compared to those obtained from a collimated on-axis illumination case. Moreover, the output LGFU waveform is essentially a merged result from two parts: a main US wave generated from the central aperture of lens and an edge wave from the rim of circular lens aperture [57]. This indicates that the main and the edge wave amplitudes would change according to the illumination beam profile on the lens aperture.

For *in-vivo* applications of our technique, LGFU amplitudes from the lens surface should be further increased to overcome acoustic attenuation through multiple tissue layers placed in typical *in-vivo* environments, for example, including skin and muscle. Moreover, US-BS signal amplitudes from a target tissue region would be proportional to the LGFU amplitude arriving at the target. The above issue should be overcome by the initial optoacoustic generation of high-pressure

amplitudes at the lens surface. This requires an improved energy conversion efficiency within the nano-composite transmitter and a high damage threshold against pulsed laser absorption. Finally, deeper tissues would lower the signal-to-noise ratio for US-BS signal acquisition. This requires advanced signal processing techniques for signal detection and differentiation especially over a frequency-spectral domain [58,59].

4. Concluding remarks

We demonstrated the broadband ultrasonic transducer designed in a hybrid manner using the PA lens to produce LGFU in which the center of lens is perforated and filled with the acoustic receiver for tissue characterization. Narrow bipolar LGFU pulses were transmitted with the center frequency of 17 MHz and the 6-dB bandwidth over 6–30 MHz, and then BS waves from the focal zone were detected by the needle-shaped piezoelectric receiver with 20-MHz bandwidth. Despite the loss in terms of transmitter area due to the perforated lens design, we confirmed that the PA lens could produce high peak amplitudes up to 48 MPa, potentially useful for therapeutic applications. Its high-frequency characteristics provided a tight focal spot size of 70 μm in lateral and 270 μm in axial dimension. We utilized the temporally narrow pulses tightly defined in space to characterize tissue elasticity and thus differentiate biological tissue types (porcine skin, muscle, and fat from belly, and rib bone). By analyzing BS signals in the frequency domain, we could characterize spectral information from the tissues in terms of mean frequency and spectral energy. The transducer capability for tissue differentiation, which is determined by elastic properties, was consistent over 2-mm depth from the tissue surface although LGFU undergoes frequency-dependent attenuation over the penetration depth. We expect that our hybrid transducer can be utilized not only for characterization of other tissue types but also for minimal-contact and non-destructive evaluation based on the elasticity of unknown materials.

Disclosures. The authors declare no conflicts of interest.

References

1. M. L. Oelze and J. Mamou, "Review of quantitative ultrasound: Envelope statistics and backscatter coefficient imaging and contributions to diagnostic ultrasound," IEEE Trans. Ultrason. Ferroelectr. Freq. Control **63**(2), 336–351 (2016).
2. C. R. Jensen, R. W. Ritchie, M. Gyöngy, J. R. Collin, T. Leslie, and C. C. Coussios, "Spatiotemporal monitoring of high-intensity focused ultrasound therapy with passive acoustic mapping," Radiology **262**(1), 252–261 (2012).
3. D. L. Miller, N. B. Smith, M. R. Bailey, G. J. Czarnota, K. Hynynen, and I. R. S. Makin, "Bioeffects Committee of the American Institute of Ultrasound in Medicine. Overview of therapeutic ultrasound applications and safety considerations," J. Ultrasound Med. **31**(4), 623–634 (2012).
4. S. B. Tajali, P. Houghton, J. C. MacDermid, and R. Grewal, "Effects of low-intensity pulsed ultrasound therapy on fracture healing: a systematic review and meta-analysis," Am. J. Phys. Med. Rehabil. **91**(4), 349–367 (2012).
5. M. S. Laasanen, S. Saarakkala, J. Töyräs, J. Hirvonen, J. Rieppo, R. K. Korhonen, and J. S. Jurvelin, "Ultrasound indentation of bovine knee articular cartilage in situ," J. Biomech. **36**(9), 1259–1267 (2003).
6. J. Mamou and M. L. Oelze, Quantitative ultrasound in soft tissues (Springer, 2013).
7. P. S. Sheeran, V. P. Wong, S. Luois, R. J. McFarland, W. D. Ross, S. Feingold, R. J. Matsunaga, and P. A. Dayton, "Decafluorobutane as a phase-change contrast agent for low-energy extravascular ultrasonic imaging," Ultrasound Med. Biol. **37**(9), 1518–1530 (2011).
8. H. Tadayyon, A. Sadeghi-Naini, L. Wirtzfeld, F. C. Wright, and G. Czarnota, "Quantitative ultrasound characterization of locally advanced breast cancer by estimation of its scatterer properties," Med. Phys. **41**(1), 012903 (2014).
9. M. C. Kolios, G. J. Czarnota, A. Worthington, A. Giles, A. S. Tunis, and M. D. Sherar, "Towards understanding the nature of high frequency backscatter from cells and tissues: An investigation of backscatter power spectra from

different concentrations of cells of different sizes," in *Proceeding of the IEEE Conference on Ultrasonics Symposium* (IEEE, 2004), pp. 606–609.

10. F. Ossant, R. Libgot, P. Coupé, P. Lermusiaux, and F. Patat, "High frequency ultrasound characterization of the coagulation process of whole blood," in *Proceeding of the IEEE Conference on Ultrasonics Symposium* (IEEE, 2004), pp. 846–849.

11. A. Ng and J. Swanevelder, "Resolution in ultrasound imaging," Continuing Educ. Anaesthesia Critic. Care Pain **11**(5), 186–192 (2011).

12. D. Dalecki, K. P. Mercado, and D. C. Hocking, "Quantitative ultrasound for nondestructive characterization of engineered tissues and biomaterials," Ann. Biomed. Eng. **44**(3), 636–648 (2016).

13. M. J. Choi, S. R. Guntur, J. M. Lee, D. G. Paeng, K. I. Lee, and A. Coleman, "Changes in ultrasonic properties of liver tissue in vitro during heating-cooling cycle concomitant with thermal coagulation," Ultrasound Med. Biol. **37**(12), 2000–2012 (2011).

14. L. Sandrin, B. Fourquet, J. M. Hasquenoph, S. Yon, C. Fournier, F. Mal, C. Christidis, M. Ziol, B. Poulet, F. Kazemi, M. Beaugrand, and M. Beaugrand, "Transient elastography: a new noninvasive method for assessment of hepatic fibrosis," Ultrasound Med. Biol. **29**(12), 1705–1713 (2003).

15. L. Sannachi, H. Tadayyon, A. Sadeghi-Naini, W. Tran, S. Gandhi, F. Wright, M. Oelze, and G. Czarnota, "Non-invasive evaluation of breast cancer response to chemotherapy using quantitative ultrasonic backscatter parameters," Med. Image Anal. **20**(1), 224–236 (2015).

16. O. Riekkinen, M. A. Hakulinen, J. Töyräs, and J. S. Jurvelin, "Dual-frequency ultrasound—new pulse–echo technique for bone densitometry," Ultrasound Med. Biol. **34**(10), 1703–1708 (2008).

17. M. A. Hakulinen, J. S. Day, J. Töyräs, M. Timonen, H. Kröger, H. Weinans, I. Kiviranta, and J. S. Jurvelin, "Prediction of density and mechanical properties of human trabecular bone in vitro by using ultrasound transmission and backscattering measurements at 0.2–6.7 MHz frequency range," Phys. Med. Biol. **50**(8), 1629–1642 (2005).

18. O. Riekkinen, M. A. Hakulinen, M. Timonen, J. Töyräs, and J. S. Jurvelin, "Influence of overlying soft tissues on trabecular bone acoustic measurement at various ultrasound frequencies," Ultrasound Med. Biol. **32**(7), 1073–1083 (2006).

19. F. Bert, J. T. Stahmeyer, and S. Rossol, "Ultrasound elastography used for preventive non-invasive screening in early detection of liver fibrosis," J. Clin. Med. Res. **8**(9), 650–655 (2016).

20. S. Gaia, S. Carenzi, A. L. Barilli, E. Bugianesi, A. Smedile, F. Brunello, A. Marzano, and M. Rizzetto, "Reliability of transient elastography for the detection of fibrosis in non-alcoholic fatty liver disease and chronic viral hepatitis," J. Hepatol. **54**(1), 64–71 (2011).

21. S. Audière, E. D. Angelini, M. Charbit, and V. Miette, "Evaluation of invivo Liver Tissue Characterization with Spectral RF Analysis versus Elasticity," in *Proceedings of International Conference on Medical Image Computing and Computer-Assisted Intervention* (Springer, 2011), pp. 387–395.

22. C. F. Braticevici, I. Sporea, E. Panaitescu, and L. Tribus, "Value of acoustic radiation force impulse imaging elastography for non-invasive evaluation of patients with nonalcoholic fatty liver disease," Ultrasound Med. Biol. **39**(11), 1942–1950 (2013).

23. H. Ochi, M. Hirooka, Y. Koizumi, T. Miyake, Y. Tokumoto, Y. Soga, F. Tada, M. Abe, Y. Hiasa, and M. Onji, "Real-time tissue elastography for evaluation of hepatic fibrosis and portal hypertension in nonalcoholic fatty liver diseases," Hepatology **56**(4), 1271–1278 (2012).

24. M. Yoneda, K. Suzuki, S. Kato, K. Fujita, Y. Nozaki, K. Hosono, S. Saito, and A. Nakajima, "Nonalcoholic fatty liver disease: US-based acoustic radiation force impulse elastography," Radiology **256**(2), 640–647 (2010).

25. A. J. Sarvazyan, T. J. Hall, M. W. Urban, M. Fatemi, S. R. Aglyamov, and B. S. Garra, "An overview of elastography-an emerging branch of medical imaging," Curr. Med. Imaging **7**(4), 255–282 (2011).

26. H. W. Baac, J. G. Ok, A. Maxwell, K. T. Lee, Y. C. Chen, A. J. Hart, Z. Xu, E. Yoon, and L. J. Guo, "Carbon-nanotube optoacoustic lens for focused ultrasound generation and high-precision targeted therapy," Sci. Rep. **2**(1), 989 (2012).

27. T. Lee, H. W. Baac, Q. Li, and L. J. Guo, "Efficient photoacoustic conversion in optical nanomaterials and composites," Adv. Opt. Mater. **6**(24), 1800491 (2018).

28. Precision Acoustics, "1-mm Needle hydrophone," https://www.acoustics.co.uk/product/1mm-needle-hydrophone/.

29. J. E. Parsons, C. A. Cain, and J. B. Fowlkes, "Cost-effective assembly of a basic fiber-optic hydrophone for measurement of high-amplitude therapeutic ultrasound fields," J. Acoust. Soc. Am. **119**(3), 1432–1440 (2006).

30. T. Lee, H. W. Baac, J. G. Ok, H. S. Youn, and L. J. Guo, "Nozzle-free liquid microjetting via homogeneous bubble nucleation," Phys. Rev. Appl. **3**(4), 044007 (2015).

31. N. Kudo, "A simple technique for visualizing ultrasound fields without Schlieren optics," Ultrasound Med. Biol. **41**(7), 2071–2081 (2015).

32. A. Gorey, S. Vasudevan, M. S. Ansari, P. Bhagat, S. Phatak, N. Sharma, and G. C. Chen, "Development of a compact laser-diode based frequency domain photoacoustic sensing system: Application of human breast cancer diagnosis," Rev. Sci. Instrum. **90**(11), 114101 (2019).

33. D. Biswas, S. Vasudevan, G. C. Chen, and N. Sharma, "Quantitative photoacoustic characterization of blood clot in blood: A mechanobiological assessment through spectral information," Rev. Sci. Instrum. **88**(2), 024301 (2017).

34. S. Karlsson and B. Gerdle, "Mean frequency and signal amplitude of the surface EMG of the quadriceps muscles increase with increasing torque—a study using the continuous wavelet transform," J. Electromyogr. Kinesiol. **11**(2), 131–140 (2001).

35. W. C. Navidi, *Statistics for engineers and scientists* (McGraw-Hill Higher Education, 2008)

36. M. Murugappan, S. Murugappan, and C. Gerard, C., "Wireless EEG signals based neuromarketing system using Fast Fourier Transform (FFT)," in *Proceeding of the IEEE Conference on 10th international colloquium on signal processing and its applications* (IEEE, 2014), pp. 25–30.

37. Y. Li, Z. Guo, G. Li, and S. L. Chen, "Miniature fiber-optic high-intensity focused ultrasound device using a candle soot nanoparticles-polydimethylsiloxane composites-coated photoacoustic lens," Opt. Express **26**(17), 21700–21711 (2018).

38. E. Aytac-Kipergil, E. J. Alles, H. C. Pauw, J. Karia, S. Noimark, and A. E. Desjardins, "Versatile and scalable fabrication method for laser-generated focused ultrasound transducers," Opt. Lett. **44**(24), 6005–6008 (2019).

39. J. Kim, W. Y. Chang, H. Wu, and X. Jiang, "Optical fiber laser-generated-focused-ultrasound transducers for intravascular therapies," In *Proceedings of IEEE Conference on International Ultrasonics Symposium* (IEEE, 2017) pp. 1–4.

40. T. Lee, W. Luo, Q. Li, H. Demirci, and L. J. Guo, "Laser-Induced Focused Ultrasound for Cavitation Treatment: Toward High-Precision Invisible Sonic Scalpel," Small **13**(38), 1701555 (2017).

41. R. S. Cobbold, *Foundations of biomedical ultrasound* (Oxford university press, 2006).

42. A. D. Maxwell, C. A. Cain, T. L. Hall, J. B. Fowlkes, and Z. Xu, "Probability of cavitation for single ultrasound pulses applied to tissues and tissue-mimicking materials," Ultrasound Med. Biol. **39**(3), 449–465 (2013).

43. E. Vlaisavljevich, K. W. Lin, A. Maxwell, M. T. Warnez, L. Mancia, R. Singh, A. J. Putnam, B. Fowlkes, E. Johnsen, C. Cain, and Z. Xu, "Effects of ultrasound frequency and tissue stiffness on the histotripsy intrinsic threshold for cavitation," Ultrasound Med. Biol. **41**(6), 1651–1667 (2015).

44. T. Lee, J. G. Ok, L. J. Guo, and H. W. Baac, "Low f-number photoacoustic lens for tight ultrasonic focusing and free-field micro-cavitation in water," Appl. Phys. Lett. **108**(10), 104102 (2016).

45. F. A. Duck, "Nonlinear acoustics in diagnostic ultrasound," Ultrasound Med. Biol. **28**(1), 1–18 (2002).

46. Y. Hou, J. S. Kim, S. W. Huang, S. Ashkenazi, L. J. Guo, and M. O'Donnell, "Characterization of a broadband all-optical ultrasound transducer-from optical and acoustical properties to imaging," IEEE Trans. Ultrason. Ferroelectr. Freq. Control **55**(8), 1867–1877 (2008).

47. G. Yoo, H. Yoon, J. Heo, U. K. Thakur, H. J. Park, H. W. Baac, and J. Heo, "All-optical ultrasound transducer using CNT-PDMS and etalon thin-film structure," IEEE Photonics J. **7**(6), 1–8 (2015).

48. R. H. Silverman, M. S. Patel, O. Gal, A. Sarup, A. Deobhakta, H. Dababneh, D. Z. Reinstein, E. J. Feleppa, and D. J. Coleman, "Effect of corneal hydration on ultrasound velocity and backscatter," Ultrasound Med. Biol. **35**(5), 839–846 (2009).

49. K. Kobayashi, S. Yoshida, Y. Saijo, and N. Hozumi, "Acoustic impedance microscopy for biological tissue characterization," Ultrasonics **54**(7), 1922–1928 (2014).

50. N. Rubert and T. Varghese, "Scatterer number density considerations in reference phantom-based attenuation estimation," Ultrasound Med. Biol. **40**(7), 1680–1696 (2014).

51. M. C. Kolios, L. Taggart, R. E. Baddour, F. S. Foster, J. W. Hunt, G. J. Czarnota, and M. D. Sherar, "An investigation of backscatter power spectra from cells, cell pellets and microspheres," In *Proceedings of IEEE Conference on International Ultrasonics Symposium* (IEEE, 2003) pp. 752–757.

52. V. R. Amin, "Ultrasonic attenuation estimation for tissue characterization," Iowa State University, Retrospective Theses and Dissertations, 17318 (1989).

53. T. Glozman and H. Azhari, "A method for characterization of tissue elastic properties combining ultrasonic computed tomography with elastography," J. Med. Ultrasound **29**(3), 387–398 (2010).

54. D. Biswas, G. C. Chen, H. W. Baac, and S. Vasudevan, "Photoacoustic Spectral Sensing Technique for Diagnosis of Biological Tissue Coagulation: In-Vitro Study," Diagnostics **10**(3), 133 (2020).

55. H. Azhari, *Basics of Biomedical Ultrasound for Engineers* (John Wiley& Sons, 2010).

56. C. M. Moran, N. L. Bush, and J. C. Bamber, "Ultrasonic propagation properties of excised human skin," Ultrasound Med. Biol. **21**(9), 1177–1190 (1995).

57. T. Lee, Y. Cheong, H. W. Baac, and L. J. Guo, "Origin of Gouy phase shift identified by laser-generated focused ultrasound," ACS Photonics **7**(11), 3236–3245 (2020).

58. Y. Ju, Z. Wei, L. Huangfu, and F. Xiao, "A new low SNR underwater acoustic signal classification method based on intrinsic modal features maintaining dimensionality reduction," Pol. Marit. Res. **27**(2), 187–198 (2020).

59. K. A. Tiwari, R. Raisutis, and V. Samaitis, "Signal processing methods to improve the Signal-to-noise ratio (SNR) in ultrasonic non-destructive testing of wind turbine blade," Procedia Struct. Integrity **5**, 1184–1191 (2017).